Received 29 April 2022; revised 20 June 2022 and 20 July 2022; accepted 24 July 2022. Date of publication 29 July 2022;
date of current version 14 October 2022. The review of this article was arranged by Editor M. Saitoh.

Digital Object Identifier 10.1109/JEDS.2022.3194120

Liquid Metal-Based Microfluidic Metasurface for Controllable Electromagnetic Wave Reflection Attenuation

XU GAO [1], PING LI [2], ZHOU YANG [1,3], LINGCHUN AN [2], ZHENHAI WANG [2], JIARUI GUO [2], NUO XU [2], AND WEI WANG [1] (Member, IEEE)

1 School of Integrated Circuits, Peking University, Beijing 100871, China
2 Applied Physics Technology Center, Beijing Institute of Mechanical Equipment, Beijing 100854, China
3 School of Engineering and Technology, China University of Geosciences (Beijing), Beijing 100083, China

CORRESPONDING AUTHORS: N. XU AND W. WANG (e-mail: xunuo26@sohu.com; w.wang@pku.edu.cn)

This work was supported by the National Natural Science Foundation of China under Grant 62074003 and Grant 82027805.
This article has supplementary downloadable material available at https://doi.org/10.1109/JEDS.2022.3194120, provided by the authors.

ABSTRACT We demonstrated a liquid metal based microfluidic chip that enabled consistent, continuous and large liquid metal unit structure array reconfiguration. The chips were assembled into a metasurface, which preliminary achieved controllable electromagnetic wave reflection attenuation. The chip contained a 5 × 6 Galinstan split-ring resonator (SRR) array, and the SRRs could be reconfigured continuously by NaOH solution pressure driven. A fin shaped microvalve was designed and integrated onto the chip, which could withstand a high fluid driving pressure (over 210 kPa), so the SRRs could be reconfigured with a large split angle. The flow resistance of each SRR chamber was analyzed for consistent and robust SRRs deformation. The SRRs enabled more than 250° reconfiguration and showed consistent deformation with a standard derivation less than 8.5°. The metasurface showed 7.5 dB and 13.5 dB attenuation at 3 GHz and 4 GHz respectively. Also, with the different split angles, there could be three attenuation peaks that reach −10 dB when the frequency ranged from 2.9-3.1 GHz, 3.7-4.2 GHz and 4.8-5.0 GHz, respectively. The metasurface we proposed can be potentially used in multiband controllable electromagnetic wave absorption.

INDEX TERMS Liquid metal, microfluidic, microvalve, reflection attenuation, metasurface.

I. INTRODUCTION

Microfluidics offers a convenient way of distributing and driving liquid, and has been widely used in the fields of sensors [1], and actuators [2], etc. Liquid metal (LM) shows great potential in microfluidics due to its high surface tension, low viscosity, and high electrical conductivity, which makes it widely used in flexible electronics [3]–[4], stretchable antenna [5], and reconfigurable metasurface [6], etc. Among all the applications, reconfigurable metasurface has become the cutting-edge research field due to its capability in dynamic electromagnetic (EM) wave response. The main approach of the mechanically reconfigurable metasurface [6] is the geometric deformation of the meta-atom [7], and LM based microfluidics has been demonstrated as an effective way to realize precise and large meta-atom reconfiguration. However, there are two main challenges to realize high performance LM based microfluidic metasurface.

Firstly, a proper way to reconfigure the LM is needed. A variety of approaches have been studied, including patterning the LM on stretchable flexible substrates [8], driven by the other fluid [9]–[12] or gravity [13], etc. Compared with the above methods, LM microfluidics based on two-phase flow provides a new strategy to achieve large, continuous and precise meta-atom reconfiguration with simple pressure control. In recent years, LM based microfluidic metasurface has been reported for many applications such as perfect absorption [9], flat lens tuning [10], beam steering [11]–[12], biosensors [14] and so on. So far, mercury (melting point −38.9°C) [9]–[10], EGaIn (melting point 15.5°C) [15] and Galinstan (melting point −19°C) [11]–[12]

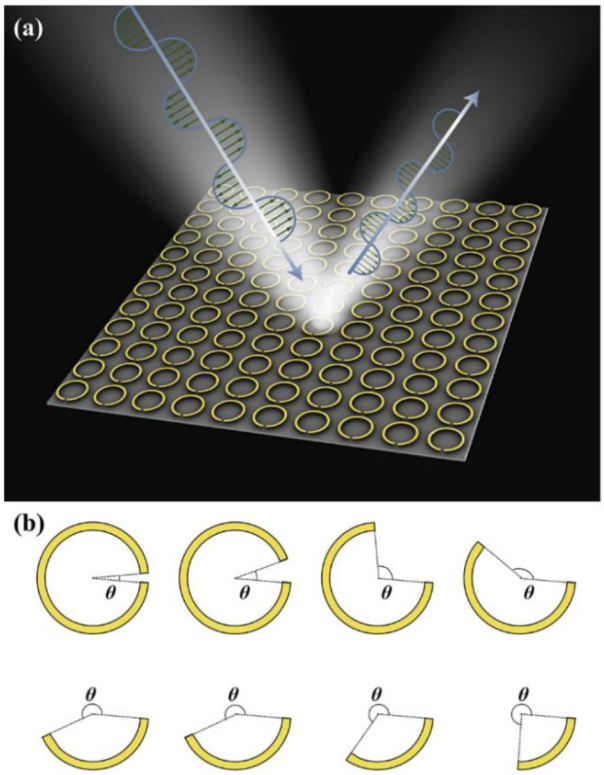

FIGURE 1. Schematic of EM wave reflection attenuator. (a) The overview of the EM wave attenuator achieved by liquid metal based microfluidic metasurface. (b) Typical shapes of the split ring, θ is the split angle.

have been commonly used in LM based microfluidic metasurface. The chemical properties of mercury are stable, so it can be driven by air [9]–[10] and many kinds of fluids. However, due to the toxicity and volatility, the safety and stability of mercury based devices are questionable. In contrast, EGaIn and Galinstan are non-toxic and non-volatile, so they are much safer and more stable, though they are very susceptible to oxidation. For EGaIn and Galinstan based devices, it is an important factor to avoid oxidation. Ga is inherently reactive. In air, the surface of EGaIn and Galinstan will generate a 1-5 nm thick solid oxidation layer [16], which will make them partial loss of liquidity and then make them harder to be driven precisely. The oxidation can be removed by strong acids or bases [16], so the HCl vapor [12] has been used in the Galinstan based LM metasurface. However, the HCl vapor is also toxic and volatile, a safe and stable LM based microfluidic metasurface must be developed. NaOH solution [5] and acidic silicone oil [17] were used to remove the oxidation layer, but due to the high viscosity of the liquid compared with air, the precise control of each meta-atom in the microfluidic metasurface calls for careful design and optimization.

Another issue required further study is the microvalve. Microvalve [18] is an important control unit microfluidic system, which mainly achieves flow control [19], fluid driving [18], and integrated microfluidic logic control [20] by changing the cross-sectional area of a flow channel. Microvalve plays an important role in the design of the LM based microfluidics metasurface. There are three key issues for microvalves applied to microfluidic metasurfaces need to be considered. Firstly, it should avoid affecting the EM resonance of meta-atoms. According to the different driving methods, microvalves can be divided into electrical, magnetic, pneumatic microvalves and so on [21]. Among them, the electrical and magnetic microvalves will introduce metal structures into the metasurface and generate conducted current and magnetic field, which will be coupled with the electric and magnetic field of the meta-atoms, so these two types of microvalves cannot be directly used in the EM responding metasurface. Pneumatic microvalve is a good choice because it does not have metal structures and does not interfering the electric and magnetic fields. Secondly, it should be capable of withstanding high driven pressure. In LM based microfluidic metasurface, the microvalve is usually used to construct the dead end of each meta-atom chamber. The LM is required to be separated into each meta-atom chamber and deformed in a certain path under stress. Larger driving pressure will cause larger deformation of meta-atom, which means more flexible EM response. However, research about microvalve performance under high driving pressure (basically more than 100 kPa) is not so much, which still a challenge to realize a high performance LM based microfluidic metasurface. Thirdly, it should be easy to realize a scale-up manufacture. Large scale integrated (LSI) microvalve array is involved in the microfluidics metasurface because there is a large number of meta-atoms that need to be manipulated. Pneumatic microvalves can be basically divided into normally open (NO) microvalves and normally closed (NC) microvalves [22], [23]. Usually, the structure of NO microvalve is much simpler, so it is widely used in LSI microfluidic systems. In contrast, NC microvalves basically contain the structure of diaphragm, which is in contact with the seat without driving pressure to interrupt the flow. It is hard to avoid the adhesion of the diaphragm to the seat during the bonding process [24]–[25], so NC microvalves are not suitable for LSI microfluidics metasurface. In short, a NO pneumatic microvalve that is endurable for high driving pressure (up to 100 kPa) should be further studied and check its applicability in liquid metal based microfluidic metasurface.

Here, we demonstrated a LM based microfluidic chip that enabled consistent, continuous and large LM unit array reconfiguration. The robust and large LM unit array reconfiguration was achieved by a novel fin shaped microvalve design. Controllable EM wave reflection attenuation was preliminarily demonstrated by using the present microfluidic chips, which contained a 5×6 reconfigurable Galinstan split-ring resonator (SRR) array. The SRRs were reconfigured by NaOH solution pressure driven flow. The concept of EM wave reflection attenuator is shown in Fig. 1(a). The shape of SRR is defined by the split angle, which means the

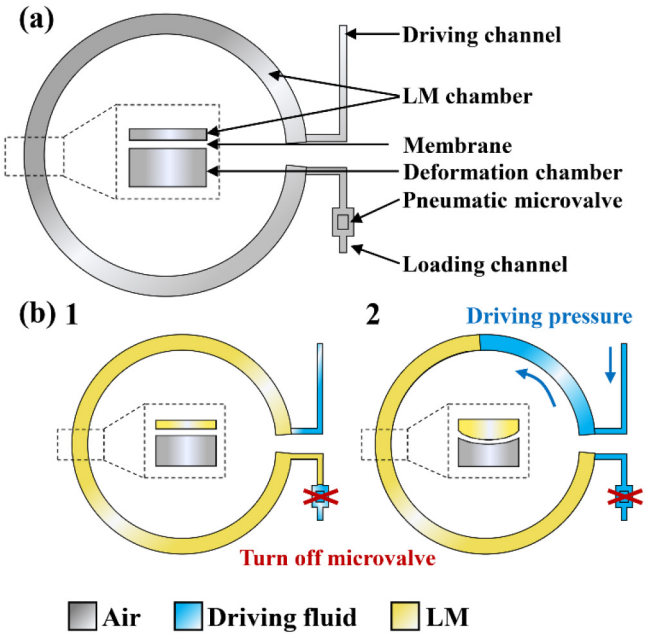

FIGURE 2. **(a) Schematic of the LM based microfluidics metasurface unit. (b) principle of the LM SRR reconfiguration.**

angle between both ends of the SRR. The typical geometry of SRR is shown in Fig. 1(b).

II. METHODS

The unit structure of the LM microfluidic chip is shown in Fig. 2(a). The chip consists of three layers. The upper layer contains the SRR-shaped LM chamber, driving channel, loading channel, and a part of the pneumatic microvalve. 4 μL Galinstan is pre-stored in each LM chamber, and the driving fluid is 1 mol/L NaOH solution for removing the oxide of Galinstan. The middle layer is an elastic membrane, whose deformation under driving pressure makes the change of geometry of SRR. The membrane is also a part of pneumatic microvalves. The lower layer contains the pneumatic channel of the microvalves. The lower layer also contains the deformation chamber, which is designed for providing space for the deformation of the membrane.

The LM SRR reconfiguring principle is shown in Fig. 2(b). After loading the Galinstan into the LM chamber, turn off the pneumatic microvalve and remove the excess Galinstan in the loading channel. Then, the Galinstan in the LM chamber can be driven by NaOH solution in the driving channel with the pneumatic microvalve keeping "off" mode. With the increasing driving pressure, the membrane will be bent downward, thereby the volume of the LM chamber will be increased. Due to the volume of the loaded LM is fixed, so the length of LM decreases, which shows the increment of split angle.

The simulations about the deformation of pneumatic microvalves and the split angle simulations were both made by COMSOL Multiphysics. Young's modulus was set as 750 kPa, and Poisson's ratio was set as 0.49. In the hyperelastic model, Mooney-Rivlin two parameters model was used. The parameter C10 was set as 293 kPa, and the C01 was set as 177 kPa. The reflectance of the EM wave attenuation was also simulated by COMSOL Multiphysics. The dielectric constant of PDMS was set as 2.65, the loss tangent delta was set as 0.04, and the electrical conductivity was set as 3.46×10^6 S/m.

The LM microfluidic chip was made of polydimethylsiloxane (PDMS). The upper and the lower PDMS layer was demoulded from the upper mold and the lower mold respectively. The molds were fabricated by a computer numerical controlled (CNC) milling machine. The middle PDMS layer was obtained by the spin coating method. These layers were bonded by Oxygen plasma treatment.

In the EM wave reflection attenuation experiment, a 30 cm × 30 cm LM microfluidic chip array was prepared. An Aluminum substrate was stuck under the LM microfluidic chip array as the perfect electric conductor layer to enhance the reflection. The chips were connected to a programable syringe pump and a pressure sensor, which made easier to control and detect the split angles of the SRR array.

III. RESULTS AND DISCUSSION

A. PERFORMANCE OF PNEUMATIC MICROVALVES

The performance of pneumatic microvalves seriously affects the robustness of the LM based microfluidic metasurface. The microvalve needs to keep "off" mode during the reconfiguration of the SRRS, which means the microvalve must strictly keep "off" mode under driving pressure more than at least 100 kPa to ensure the large deformation of SRRs. Once the microvalve cannot keep "off" mode under driving pressure, the LM will flow out of the chamber, which will cause the defects of the SRRs and then the EM resonance of the SRRs will be affected. What's more, due to the bonding strength of the chip is limited, the ratio of the withstandable driving pressure ΔP_d and the turn-off pressure ΔP_t should be as high as possible to achieve higher ΔP_d. Therefore, an easy to fabricate and operate microvalve which can completely interrupt the flow with high $\Delta P_d/\Delta P_t$ should be considered.

We firstly compared 3 types of traditional NO microvalves, rectangular cross shaped [18], flat slope shaped [26], and rounded slope shaped [18] microvalves, respectively. The minimum height of the microvalve chamber along the middle line of the flow channel was 100 μm, 100 μm and 50 μm, respectively. The microvalve chambers were all 1 mm in length and 0.8 mm in width. 60 kPa pressure was applied to the wall of the pneumatic channel. The Von-mises stress distribution of these 3 types of microvalves is shown in the first row of Fig. 3(a)-(c). The contact stress distribution and the membrane deformation of these 3 types of microvalves are shown in the second row of Fig. 3(a)-(c). The rectangular cross shaped, flat slope shaped microvalves could not be closed completely because the membrane could not fully contact the corner of the top surface. The rounded slope

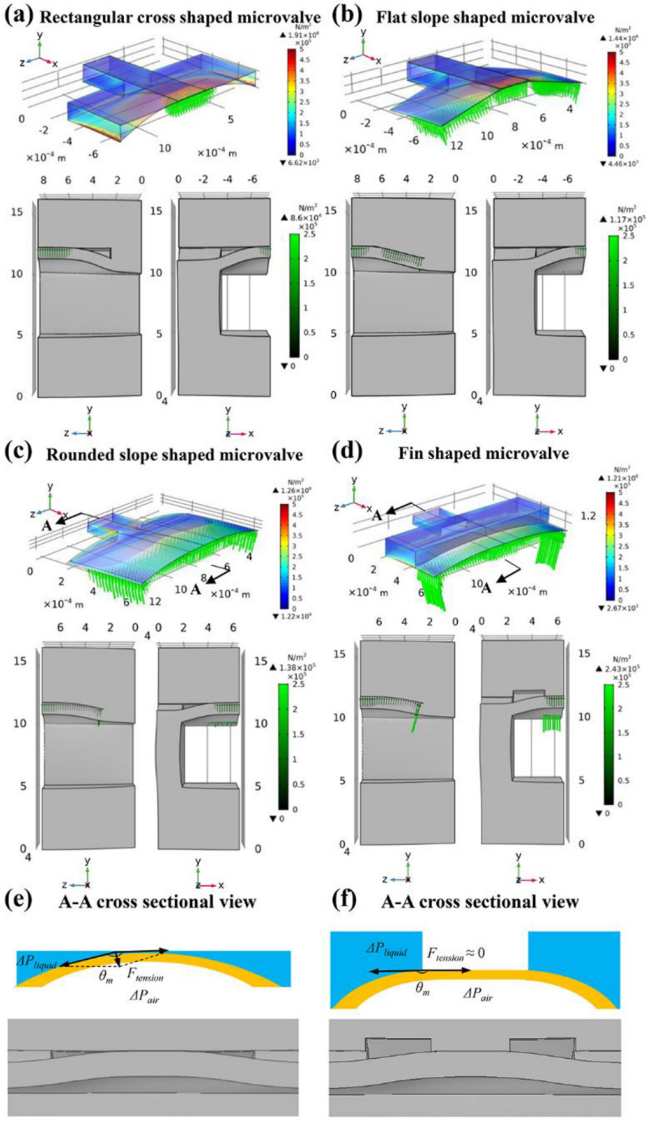

FIGURE 3. **Optimal design of the microfluidic microvalve. (a)-(d) Simulation results of Von-mises stress distribution, contact stress distribution and the deformation of the membrane under 60 kPa pressure load for rectangular cross shaped, flat slope shaped, rounded slope shaped and fin shaped microvalve, respectively. (e)-(f) Comparison of the forces applied to the contact line of the rounded slope shaped and the fin shaped microvalve from A-A cross sectional view, respectively.**

shaped could be closed completely because the curvature of the top surface is close to the curvature of deformed membrane. The A-A cross sectional view of the rounded slope shaped microvalve is shown in Fig. 3(e). The membrane contact angle θ_m was defined as the angle between the interface of the liquid-membrane and the top wall. In the rounded slope shaped microvalve model, the θ_m was less than 180°, so the resultant force of the tension of the membrane $F_{tension}$ would hinder the close of the microvalve. If the θ_m could be equal to or more than 180°, the $F_{tension}$ would have no effect or promote the close of the microvalve.

TABLE 1. **Pneumatic microvalve designs related to this work.**

Work	Type	Materials	Size (mm)	W_{min} (μm)	T_m (μm)	Chip/mould fabrication	$\Delta P_d/\Delta P_t$ ΔP_t (kPa)
[27]	NC	PDMS Glass	D=1.5	100	254	Lithography	1.75 ~10-40
[28]	NC	PMMA PDMS	/	/	/	Laser ablation	1.80 25
[18]	NO	Silicon rubber	L=0.1 W=0.1	100	30	Lithography (mould)	0.41 170
[23]	NO	PMMA FEP	L=0.3 W=0.3	300	12.5	CNC milling	0.50 200
[24]	NO	Glass PDMS	D=1.0	~0	250	Lithography	1.33 ~50-160
This work	NO	PDMS	L=1.2 W=1.0	200	100	CNC milling (mould)	0.98 ~70-210

Therefore, we proposed the design of the fin shaped microvalve. Compared with the rounded slope shaped microvalve, the fin shaped microvalve was introduced a fin shaped step to offer more space for the membrane to achieve full deformation once the central part of the membrane was in contact with the step. Further deformation of the membrane on both sides of the step enabled a larger θ_m, which could achieve higher $\Delta P_d/\Delta P_t$. The Von-mises stress distribution and the contact stress distribution of the fin shaped microvalve are shown in Fig. 3(d). The membrane could be fully in contact with the step. The A-A cross sectional view of the fin shaped microvalve is shown in Fig. 3(f). The θ_m was near 180°, which meant the $\Delta P_d/\Delta P_t$ might be near 1.

To verify the performance of the above designs, flat slope shaped, rounded slope shaped and fin shaped microvalves were fabricated and tested. The thickness of the membrane was 100 μm. The shapes of the contact surface with increasing load pressure of these 3 types are shown in Fig. 4(a)-(c). The observed shape of the contact surface was the same as the simulation results. The fin shaped microvalve showd the best turn-off performance. The relationship between the ΔP_t and the ΔP_d of the fin shaped microvalve is shown in Fig. 4(d). Only if the turn-off pressure was higher than 70 kPa, the fin shaped microvalve could totally interrupt the pressure driven flow. The $\Delta P_d/\Delta P_t$ was near 0.98 which shows the good performance of the microvalve, and it also matched the previous prediction.

Table 1 shows several microvalve designs related to our work. The NC microvalves [27]–[28] enable more than 1 $\Delta P_d/\Delta P_t$ under the respectively listed ΔP_t. However, these two types of NC microvalves are quite hard to be integrated into the LM based microfluidic metasurface. Also, the work [27] shows that the ΔP_d cannot increase further when the ΔP_t is higher than 40 kPa which means the performance of NC microvalve under high ΔP_t needs to be studied further. The rounded slope shaped NO microvalve [18] only achieves 0.41 $\Delta P_d/\Delta P_t$ under 170 kPa, which means only ensuring the full contact between the membrane and the top surface is not enough, the θ_m of the deformed membrane is crucial, so the introduction of fin shaped step is helpful for increasing the $\Delta P_d/\Delta P_t$. The NO microvalve [24] is the

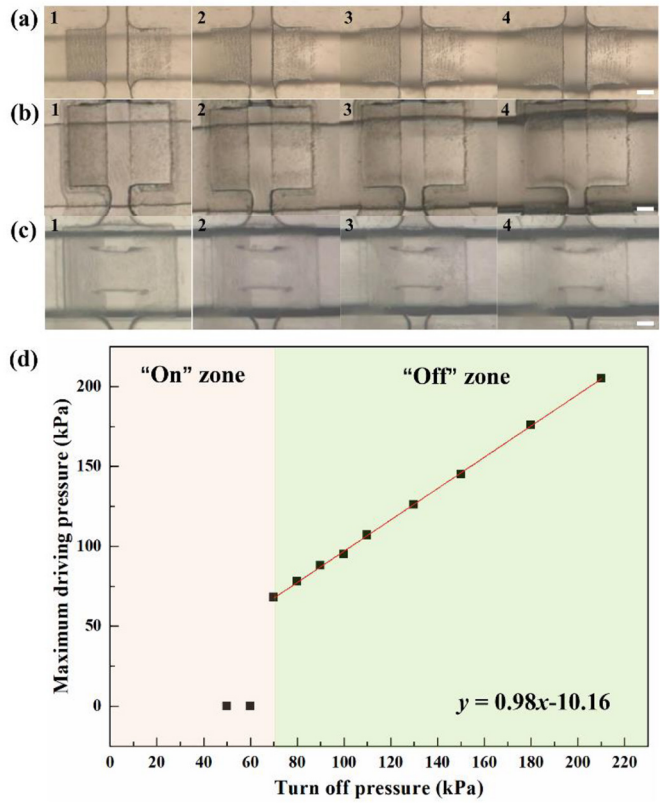

FIGURE 4. **(a)-(c) The shape of the contact surface with increasing load pressure of the flat slope shaped, rounded slope shaped and fin shaped valve, respectively. (d) Relationship of the turn-off pressure and the maximum driving pressure of the fin shaped valve. All scale bars are 200 μm.**

combination of design ideas of NC and NO microvalves, ~0 μm thick diaphragm is made by isotropic glass etching, and the distance between the diaphragm and the seat is 5 μm. It shows quite good $\Delta P_d/\Delta P_t$ with ΔP_t up to 160 kPa. However, the fabrication of the microvalve array needs to be precisely controlled, so the microvalve is difficult to be integrated with the LSI flow network. Another big problem with the above three designs [24], [27]–[28] is that mass production is quite costly, which will limit the application of the microfluidic metasurface with large area, for example, stealth surface. The fin shaped microvalve we proposed introduces lateral curvature and longitudinal step of the top surface. The lateral curvature allows the membrane to fit the upper surface sufficiently under pressure, so it can decrease the ΔP_t. The longitudinal step offers more space for the membrane to deform which enables near 180° θ_m, so it could increase the $\Delta P_d/\Delta P_t$. The fin shaped microvalve is made by PDMS, which means the multilayers can be mass-produced by demoulding method. Also, a 50 μm distance between the membrane and the bottom surface of the fin makes the risk of bonding failure significantly reduced. Therefore, the fin shaped microvalve we proposed is a good design for LSI microfluidic system which is suitable for working under high driving pressure. The effect of the width of the fin on the maximum $\Delta P_d/\Delta P_t$ that enables the totally close of the microvalve needs to be studied further.

B. CONSISTENT OF SRRs

Consistent deformation of each LM SRR under the same driving pressure is crucial because it's the basis of precise SRR array control. The flow resistance of the flow channel network needs to be considered during the chip design, which highly affects the consistency of the SRRs.

The schematic of the simplified flow channel is shown in Fig. 5(a). The LM is stored in the LM chamber, with one dead-end, and the other end is connected to the driving channel. Its equivalent flow resistance network is shown in Fig. 5(b). R_1 to R_5 represent the flow resistance of each section of the channel respectively. Q_1 to Q_3 represent the flow of each branch respectively. The deformable LM chambers 1-3 are equivalent to C_1 to C_3 respectively because the process of storing and releasing liquid for the elastic LM chamber is quite similar to the process of charging and discharging for the capacitor. P_{load1} to P_{load3} represent the pressure loaded on C_1 to C_3 respectively, which are mainly affected by the tensor of the middle layer.

The difference between P_{load1} to P_{load3} will cause different split angles. If P_{in} is a constant, there is

$$P_{load1} = P_{load2} = P_{load3} = P_{in} \tag{1}$$

That means the consistency of the SRRs is mainly affected by fabrication and operation errors. For example, if the LM chamber and the air chamber are not in good alignment, the area of the membrane that induced the deformation will be different in each unit. The initial volume of LM in each chamber will also cause the difference of split angle under the same pressure. If we consume that P_{in} is a function of sinusoidal variation

$$P_{in} = P_{max} sin\omega t \tag{2}$$

P_{max} is the amplitude of P_{in}, P_{load1} to P_{load3} can be derived as:

$$P_{load1} = \frac{P_{in}}{R_1\omega C_1 + 1} \tag{3}$$

$$P_{load2} = \frac{P_{in}}{(R_2 + R_4)\omega C_2 + 1} \tag{4}$$

$$P_{load3} = \frac{P_{in}}{(R_3 + R_4 + R_5)\omega C_3 + 1} \tag{5}$$

To ensure that a greater proportion of P_{in} can be applied to each SRR, decreasing the flow resistance of the flow network, and decreasing the rate of pressure change can improve the consistency of SRRs. Although decreasing the C_1 to C_3 can increase the P_{load1} to P_{load3}, it means the limited capacity to store the liquid in each SRR, which will decrease the maximum split angle. Pressure drop in each section of the channel can be calculated according to the Hagen-Poiseuille equation:

$$\Delta P = \frac{32\mu l v}{D^2} \tag{6}$$

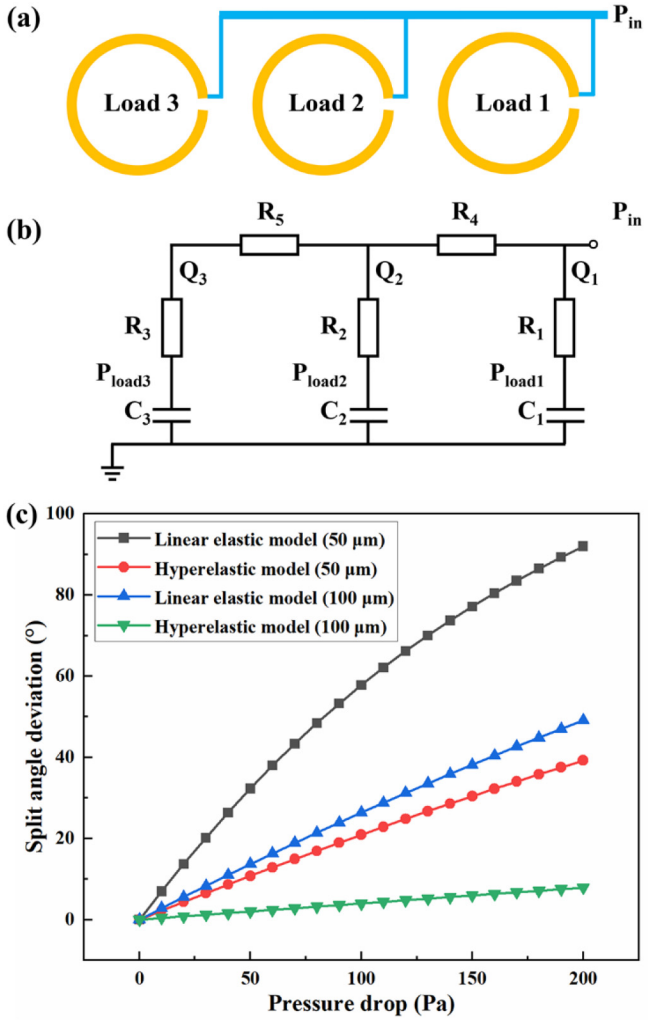

FIGURE 5. (a) Schematic of the pressure distribution of the flow channel. (b) Equivalent flow resistance network of the flow channel. (c) Simulation results about the relationship between pressure drop and the difference of split angle.

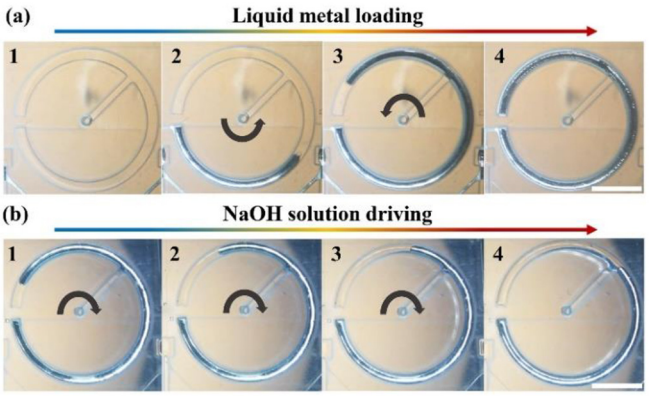

FIGURE 6. Backside view under microscope of LM loading and driving process and results. (a) LM loading process. (b) LM driving process. All scale bars are 5 mm.

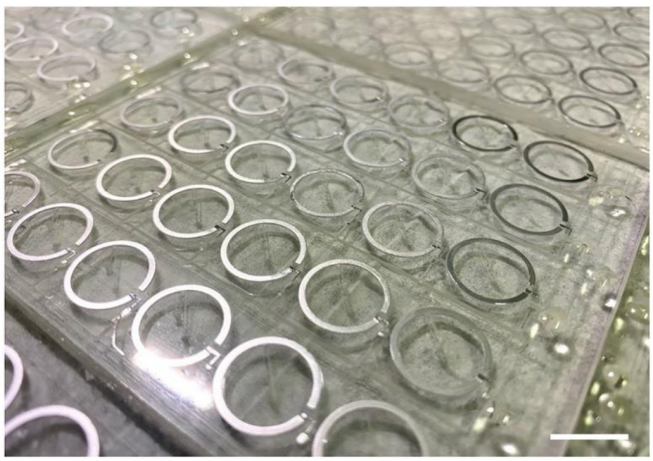

FIGURE 7. LM based microfluidics chips array. Scale bar is 10 mm.

Here, μ is the dynamic viscosity, l is the length of the channel, v is the velocity of flow, D is the hydraulic diameter. For a $D = 0.2$ mm, $v = 1$ cm/s, $\mu = 1$ mPa·s channel, there is an 80 Pa pressure drop in 1 cm length.

Simulation results about the relationship between the pressure and the split angle deviation are shown in Fig. 5(c). There was a 20° and 2° deviation for 50 μm and 100 μm thick middle layer under the hyperelastic hypothesis when the pressure drop between two SRRs came to 100 Pa. In the Galintan and NaOH solution system, the pressure drop is directly affected by driving speed v. Therefore, the balance between the limited driving speed and the accuracy of the split angle control needs to be considered. To ensure the accuracy of the split angle control, 100 μm thick middle layer was used in this work.

C. SRRS RECONFIGURATION

The process of LM loading is shown in Fig. 6(a). In the LM loading process, Galinstan was loaded through the loading channel to fill the LM chamber with the microvalve in "on" mode. The LM chamber was preloaded with the NaOH solution to avoid the oxidation of Galinstan. Therefore, the flow of Galinstan in the channel exhibited the characteristics of an ideal fluid. No adhesion of oxide on the channel wall was observed. The graphs of the deformation of the SRR are shown in Fig. 6(b). The microvalve was in "off" mode, and the NaOH solution was pushed into the LM chamber under driving pressure. Due to the Galinstan was trapped in the LM chamber, with the increment of driving pressure, the membrane was deformed, so the fraction of Galinstan in the LM chamber was decreased which shows the increment of split angle. The SRR can be reconfigured stably and continuously without the leakage of Galinstan, which shows the good performance of the fin shaped pneumatic microvalve.

The fabricated LM microfluidic chip array is shown in Fig. 7. The chip was 110 mm in length and 95 mm in width. The SRR was 14 mm in diameter, and the initial split angle was 10°. The graphs of the SRRs which are in one row in different states are shown in Fig. 4(a). In

each SRR, the angle between two solid arrows represents the measured split angle, and the angle between the dotted line and the solid arrow in the fixed position represents the mean split angle. The standard deviation of measured split angles was near 8.5°, which indicated good consistency of the SRR array. We recorded the driving pressure in different liquid feeding modes, which was shown in Fig. 8(b). With the same volume of the driving fluid input under different loading speeds, the pressure kept the same, which also meant the split angles of the SRRs kept the same. It showed that the chip enabled reversible and repeatable SRR array deformation. However, we noticed that in each pressure step, there was always a pressure spike at the beginning, and then the pressure went down to the plateau stage gradually. It may have several reasons. Firstly, for a stationary fluid network, due to the inertial force, the sudden feeding of the driving fluid will cause a pressure spike. The faster the driving fluid is fed, the higher the pressure spike will be. Secondly, the reconfiguration process of the SRRs is caused by the elastic deformation of the PDMS membrane and the distribution of the driving fluid in each LM chamber. It means that when the driving pressure is applied to the chip, the chip requires a certain response time to reach its stable state. During the experiment, the same volume of driving fluid was fed, and the chip pressure could be stabilized at the same value, which showed that there was no obvious pressure drop in the chip. Details about pressure fluctuations need to be discussed further. The split angles of the SRRs did not seriously fluctuate with the fluctuation of pressure. Supplementary Video S1 shows the dynamic variation of the SRR array under pressure-driven. The split angles stayed stable 5 s after driving fluid feeding. The variation of the split angle during pressure fluctuation was less than 5°. The simulated and measured results about the relationship between the driving pressure and the split angle are shown in Fig. 8(c). The measured results were close to the simulation results under the hyperelastic hypothesis when the split angle was less than 200°, and were closer to the results under the linear elastic hypothesis when the split angle was more than 200°. This is good guidance for membrane deformation based PDMS devices.

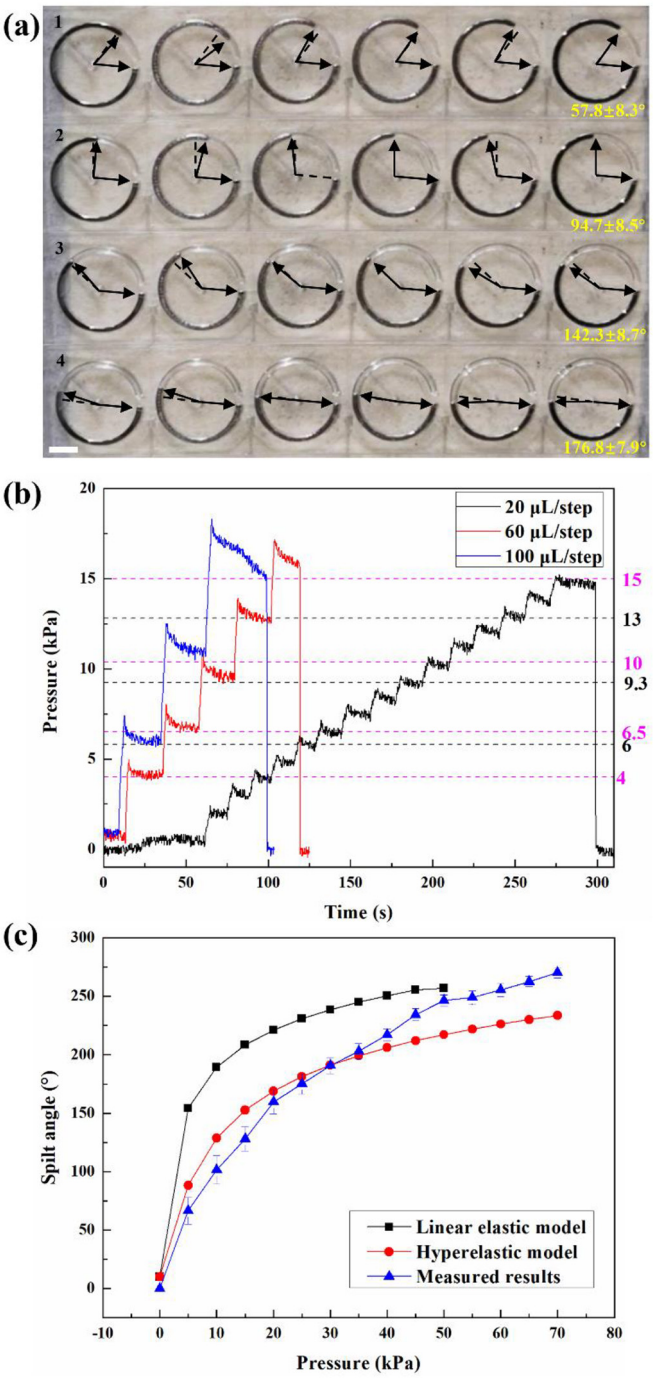

FIGURE 8. **(a) Graphs of the SRRs in different shapes with high consistency. (b) Pressure curve in different injection step modes. (c) Simulation and experiment results of the relationship split angle is less than 200°, and are closer to the results under between driving pressure and split angle. Scale bar is 5 mm.**

D. EM WAVE REFLECTION ATTENUATION

Reflection attenuation is widely used in EM wave absorption [29]–[31]. We preliminary explored the potential application of LM microfluidic chips in controllable EM wave reflection attenuation. Based on the LM microfluidic chip, EM wave reflection attenuation was tested in a microwave anechoic chamber. The measured and simulation results with split angles of 45°, 90°, and 135° are shown in Fig. 9 (a)-(c) respectively. The insets show the simulated near field electrical field with the corresponding split angle at the frequency 4.6 GHz, 4.1 GHz, and 3.1 GHz respectively, which show the greatest resonance in simulation results from 2 GHz to 8 GHz. In the range of 45° to 135° of the split angle, the measured reflectivity had the trend of attenuating with the increment of the split angle at 3 GHz, and with the decrement of the split angle at 4 GHz. There was 7.5 dB and 13.5 dB attenuation at 3 GHz and 4 GHz respectively, which validated

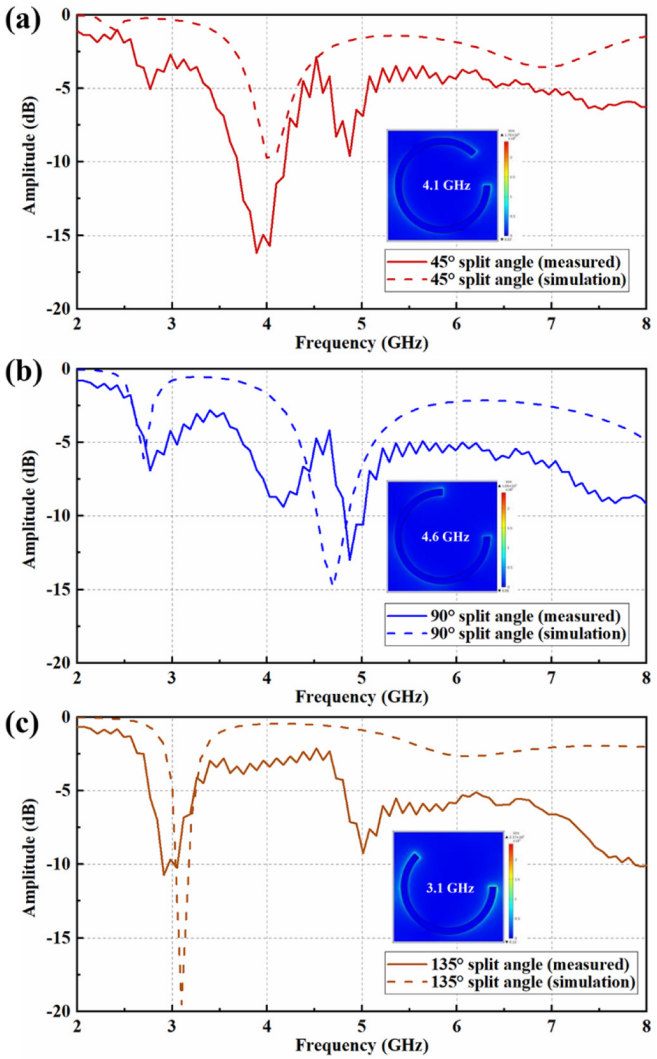

FIGURE 9. **The Measured and simulation results of the EM wave attenuator. (a)-(c) The measured (solid line) and simulation (dashed line) results with 45°, 90°, and 135° split angle, respectively. Each inset shows the near-field electrical field at the frequency which enables minimum amplitude.**

the regulation of the dynamic response of EM wave reflection by the LM microfluidic metasurface. Moreover, with the different split angles, there could be three attenuation peaks reach −10 dB (effective absorption bandwidth [32]) when the frequency ranged from 2.9-3.1 GHz, 3.7-4.2 GHz and 4.8-5.0 GHz, respectively. Compared with the previous metasurface research about multiband attenuators [31], the metasurface we proposed can be a selective multiband attenuator with more than 90% absorption at S-band and C-band. The difference between the measured results and the simulated results might be because of the introduction of NaOH solution which is electrically conductive. The increasing span size of SRRs at the edge of the chip might also induce the unideal EM resonance.

IV. CONCLUSION

In this work, we demonstrated a LM based microfluidic chip. A robust fin shaped pneumatic microvalve for stably loading and separation of LM was designed. It achieves 0.98 $\Delta P_d/\Delta P_t$, and the ΔP_d can be up to 210 kPa, which shows a good tolerance of driving pressure. We also discussed the design principles that affected the stability and consistency of the SRR array. The chip enables ±8.5° deformation of the SRR array. The chip array preliminary shows the potential in EM wave reflection attenuation at 3 GHz and 4 GHz. In the future, precise geometry control will make this method have the potential to achieve more accurate EM wave moderation. We will do more work on the EM performance of the chip, such as the sensitivity of the incident angle. Optimization of the structure of SRRs to achieve a broadband attenuator will be studied in the future. Future, many types of reconfigurable metasurfaces will be designed.

At present, there are still some problems in this work that need to be improved. For the mass production of large-area LM based microfluidic metasurface, the manufacturing consistency requires further improvement, especially the alignment bonding process. Alignment bonding of the large area flexible material such as PDMS is a challenge because the layers might not be flat enough to be precisely aligned and the micro-structure might be deformed under stress. Unideal alignment can increase the ΔP_t of microvalves, which might cause the LM leakage during the driving process. The air permeability of the PDMS chip is the other problem, which makes it difficult for the microvalve to maintain turn off pressure for a long time, so this will affect the long-term stability of the metasurface. Compared with common barrier layer like glass or Parylene C, Parylene C-caulked PDMS [33]–[34] will be an efficient solution because the barrier layers are hard to fully cover the chip. Reducing the permeability of the chip can also reduce the reaction of Galinstan with oxygen, thereby slowing or even avoiding the production of oxidation. If the generation of oxidation is avoided, Galinstan will be able to be driven by a variety of fluids, such as fluorinated fluids, silicone oils, nitrogen, and so on.

Moreover, due to the high surface tension of LM, it's difficult to construct the reconfigurable resonators with an overall size smaller than 1 mm, which also requires large and continuous deformation, so the LM based microfluidics can mainly be used in the GHz band basically. The oxidation of Galinstan is also a big challenge. We use NaOH solution to remove the oxide, but the generation of reaction products and the loss of the water are unavoidable. Therefore, driving strategies for microscale LM structure and robust chip materials need to be considered in the future.

APPENDIX

Supplementary Video S1 shows the dynamic variation of the split angles of the SRRs.

ACKNOWLEDGMENT

The authors gratefully acknowledge the contributions of Dr. Teng Chen for his help with the experiment of EM wave reflection attenuation. Portions of this work were published at the 6th IEEE Electron Devices Technology and Manufacturing (EDTM) Conference 2022. The title of the paper is "Liquid metal microfluidic electromagnetic wave reflection attenuator" (DOI: 10.1109/EDTM53872.2022.9798211).

REFERENCES

[1] R. Funari, K.-Y. Chu, and A. Q. Shen, "Detection of antibodies against SARS-CoV-2 spike protein by gold nanospikes in an opto-microfluidic chip," *Biosens. Bioelectron.*, vol. 169, no. 1, Dec. 2020, Art. no. 112578, doi: 10.1016/j.bios.2020.112578.

[2] J. H. Ha *et al.*, "Electro-responsive hydrogel-based microfluidic actuator platform for photothermal therapy," *Lab Chip*, vol. 20, pp. 3354–3364, Aug. 2020, doi: 10.1039/d0lc00458h.

[3] Y. Gao *et al.*, "Wearable microfluidic diaphragm pressure sensor for health and tactile touch monitoring," *Adv. Mater.*, vol. 29, no. 39, Oct. 2017, Art. no. 1701985, doi: 10.1002/adma.201701985.

[4] Y. Liu *et al.*, "Ultrastretchable and wireless bioelectronics based on all-hydrogel microfluidics," *Adv. Mater.*, vol. 31, no. 39, Sep. 2019, Art. no. 1902783, doi: 10.1002/adma.201902783.

[5] R. C. Gough, A. M. Morishita, J. H. Dang, W. Hu, W. A. Shiroma, and A. T. Ohta, "Continuous electrowetting of non-toxic liquid metal for RF applications," *IEEE Access*, vol. 2, pp. 874–882, 2014, doi: 10.1109/ACCESS.2014.2350531.

[6] Q. He, S. Sun, and L. Zhou, "Tunable/reconfigurable metasurfaces: Physics and applications," *Research*, vol. 2019, Jul. 2019, Art. no. 1849272, doi: 10.34133/2019/1849272.

[7] N. Meinzer, W. L. Barnes, and I. R. Hooper, "Plasmonic meta-atoms and metasurfaces," *Nat. Photon.*, vol. 8, pp. 889–898, Nov. 2014, doi: 10.1038/nphoton.2014.247.

[8] P. Liu *et al.*, "Tunable meta-atom using liquid metal embedded in stretchable polymer," *J. Appl. Phys.*, vol. 118, Jul. 2015, Art. no. 14504, doi: 10.1063/1.4926417.

[9] Q. H. Song *et al.*, "Liquid-metal-based metasurface for terahertz absorption material: Frequency-agile and wide-angle," *APL Mater.*, vol. 5, no. 6, May 2017, Art. no. 66103, doi: 10.1063/1.4985288.

[10] W. Zhu *et al.*, "A flat lens with tunable phase gradient by using random access reconfigurable metamaterial," *Adv. Mater.*, vol. 27, no. 32, pp. 4739–4743, Aug. 2015, doi: 10.1002/adma.201501943.

[11] L. Yan *et al.*, "Arbitrary and independent polarization control in situ via a single metasurface," *Adv. Opt. Mater.*, vol. 6, no. 21, Nov. 2018, Art. no. 1800728, doi: 10.1002/adom.201800728.

[12] P. C. Wu *et al.*, "Broadband wide-angle multifunctional polarization converter via liquid-metal-based metasurface," *Adv. Opt. Mater.*, vol. 5, no. 7, Feb. 2017, Art. no. 1600938, doi: 10.1002/adom.201600938.

[13] T. Qian, "Reconfigurable metasurface antenna based on the liquid metal for flexible scattering fields manipulation," *Micromachines*, vol. 12, no. 3, p. 243, Feb. 2021, doi: 10.3390/mi12030243.

[14] A. Ebrahimi, J. Scott, and K. Ghorbani, "Microwave reflective biosensor for glucose level detection in aqueous solutions," *Sens. Actuat. A, Phys.*, vol. 301, Jan. 2020, Art. no. 111662, doi: 10.1016/j.sna.2019.111662.

[15] S. Ghosh, and S. Lim, "Fluidically switchable metasurface for wide spectrum absorption," *Sci. Rep.*, vol. 8, Jul. 2018, Art. no. 10169, doi: 10.1038/s41598-018-28574-9.

[16] S.-Y. Tang, C. Tabor, K. Kalantar-Zadeh, and M. D. Dickey, "Gallium liquid metal: The devil's elixir," *Annu. Rev. Mater.*, vol. 51, pp. 381–408, Jul. 2021, doi: 10.1146/annurev-matsci-080819-125403.

[17] A. V. Diebold *et al.*, "Electrowetting-actuated liquid metal for RF applications," *J. Micromech. Microeng.*, vol. 27, Jan. 2017, Art. no. 25010, doi: 10.1088/1361-6439/aa556a.

[18] M. A. Unger, H.-P. Chou, T. Thorsen, A. Scherer, and S. R. Quake, "Monolithic microfabricated valves and pumps by multilayer soft lithography," *Science*, vol. 288, no. 5643, pp. 113–116, Apr. 2000, doi: 10.1126/science.288.5463.113.

[19] I. Doh and Y.-H. Cho, "Passive flow-rate regulators using pressure-dependent autonomous deflection of parallel membrane valves," *Lab Chip*, vol. 9, pp. 2070–2075, Mar. 2009, doi: 10.1039/B821524C.

[20] K. Kawai, K. Arima, M. Morita, and S. Shoji, "Microfluidic valve array control system integrating a fluid demultiplexer circuit," *J. Micromech. Microeng.*, vol. 25, May 2015, Art. no. 65016, doi: 10.1088/0960-1317/25/6/065016.

[21] J.-Y. Qian, C.-W. Hou, X.-J. Li, and Z.-J. Jin, "Actuation mechanism of microvalves: A review," *Micromachines*, vol. 11, no. 2, p. 172, Jan. 2020, doi: 10.3390/mi11020172.

[22] R. Mohan, B. R. Schudel, A. V. Desai, J. D. Yearsley, C. A. Apblett, and P. J. A. Kenis, "Design considerations for elastomeric normally closed microfluidic valves," *Sens. Actuat. B, Chem.*, vol. 160, no. 1, pp. 1216–1223, Dec. 2011, doi: 10.1016/j.snb.2011.09.051.

[23] S. S. Huang, Q. He, H. Chen, and J. Huang, "Preparation of normally open microvalves with fluorinated ethylene propylene membrane and poly(methyl methacrylate) substrates," *Microfluid Nanofluidics*, vol. 14, pp. 329–335, Sep. 2013, doi: 10.1007/s10404-012-1052-1.

[24] C.-S. Park *et al.*, "A PDMS membrane microvalve with one-dimensional line valve seat for robust microfluidics," *J. Micromech. Microeng.*, vol. 24, no. 2, Jan. 2014, Art. no. 27002, doi: 10.1088/0960-1317/24/2/027002.

[25] A. Jahanshahi, P. Salvo, and J. Vanfleteren, "PDMS selective bonding for the fabrication of biocompatible all polymer NC microvalves," *J. Microelectromech. Syst.*, vol. 22, no. 6, pp. 1354–1360, Dec. 2013, doi: 10.1109/JMEMS.2013.2262595.

[26] M. Kaminaga, T. Ishida, and T. Omata, "Microvalve with trapezoid-shaped cross-section for deep microchannels," *Micromachines*, vol. 12, no. 11, p. 1403, Nov. 2021, doi: 10.3390/mi12111403.

[27] W. H. Grover, A. M. Skelley, C. N. Liu, E. T. Lagally, and R. A. Mathies, "Monolithic membrane valves and diaphragm pumps for practical large-scale integration into glass microfluidic devices," *Sens. Actuat. B, Chem.*, vol. 89, no. 3, pp. 315–323, Apr. 2003, doi: 10.1016/S0925-4005(02)00468-9.

[28] W. H. Zhang *et al.*, "PMMA/PDMS valves and pumps for disposable microfluidics," *Lab Chip*, vol. 9, pp. 3088–3094, Aug. 2009, doi: 10.1039/B907254C.

[29] Y. Fan *et al.*, "Ultra-thin and -broadband microwave magnetic absorber enhanced by phase gradient metasurface incorporation," *J. Phys. D, Appl. Phys.*, vol. 51, no. 21, May 2018, Art. no. 215001, doi: 10.1088/1361-6463/aab8cd.

[30] X. M. Fu *et al.*, "Ultra-wideband microwave absorber via an integrated metasurface and impedance-matching lattice design," *J. Phys. D, Appl. Phys.*, vol. 52, no. 31, Jun. 2019, Art. no. 31LT01, doi: 10.1088/1361-6463/ab2030.

[31] S. Charola, S. K. Patel, J. Parmar, and R. Jadeja, "Multiband Jerusalem cross-shaped angle insensitive metasurface absorber for X-band application," *J. Electromagn. Waves Appl.*, vol. 36, no. 2, pp. 180–192, Aug. 2021, doi: 10.1080/09205071.2021.1960643.

[32] A. Ling *et al.*, "Broadband microwave absorbing materials based on MWCNTs' electromagnetic wave filtering effect," *Compos. B, Eng.*, vol. 171, no. 15, pp. 214–221, Aug. 2019, doi: 10.1016/j.compositesb.2019.04.034.

[33] Y. Lei, Y. Liu, W. Wang, W. Wu, and Z. Li, "Studies on Parylene C-caulked PDMS (pcPDMS) for low permeability required microfluidics applications," *Lab Chip*, vol. 11, no. 7, pp. 1385–1388, Feb. 2011, doi: 10.1039/C0LC00486C.

[34] Y. Liu, L. Zhang, C. Mo, Y. Cao, W. Wu, and W. Wang, "Caulking polydimethylsiloxane molecular networks by thermal chemical vapor deposition of Parylene-C," *Lab Chip*, vol. 16, no. 21, pp. 4220–4229, Sep. 2016, doi: 10.1039/C6LC01086E.